Embedded Metasurfaces for Robust and Orientation-Independent Imaging Applications

*Zixuan Wang, Chuang Sun, Kian Shen Kiang, Jun-Yu Ou, and Jize Yan**

Zixuan Wang, Chuang Sun, Kian Shen Kiang, Jize Yan
School of Electronics and Computer Science, University of Southampton, Southampton, UK
E-mail: J.Yan@soton.ac.uk

Jun-Yu Ou
Department of Physics and Astronomy, University of Southampton, Southampton, UK

Funding: This work was supported by the UK's Engineering and Physical Sciences Research Council (project number EP/V000624/1).

Keywords: Metasurface, Conformal Layer, Mechanical Stability, Orientation-Independent Optics

Abstract

Metasurfaces offer compact, lightweight alternatives to conventional optics by enabling precise wavefront control with subwavelength nanostructures. However, the mechanical fragility of pillar-based configurations limits their applicability in practical systems, particularly under routine handling and cleaning. Here, we report a mechanically robust metasurface architecture in which high refractive index nanopillars are encapsulated within a conformal SiO_2 layer. Numerical simulations indicate that the embedded design maintains stable focusing efficiency over a wide range of surrounding refractive index values of common operational media such as air, water, and oil, whereas pillar-based structures exhibit significant degradation. Experimentally, the embedded design preserves diffraction-limited focusing and high-contrast imaging performance. After standard mechanical cleaning, the embedded metasurface maintains over 90% of its initial focusing efficiency, while unprotected metasurfaces exhibit an efficiency reduction of approximately 88%. The near-symmetric dielectric layer enhances orientation-independent optical response, demonstrating identical imaging performance under forward and reverse illumination. A magnification ratio of 1.29 is observed between two configurations. This ratio arises from the difference in object distances, which is caused by the thickness differences in the substrate and the encapsulated

SiO_2 layer. This CMOS-compatible, bidirectional, and mechanically stable metasurface platform provides a scalable approach to integrated flat optics for advanced imaging and sensing applications.

1. Introduction

Metasurfaces—planar optical components composed of subwavelength-scale nanostructures—have emerged as compact and lightweight alternatives to conventional bulk optics.[1] By precisely engineering the geometry and spatial distribution of constituent meta-atoms, these surfaces enable full control over amplitude, phase, polarization, and frequency,[2–5] facilitating a wide range of functions including wavefront shaping,[2,7,8] structured beam generation,[9] holography,[10–14] polarization control,[9,15–17] and advanced spectroscopy.[18–22] Metalenses based on hyperbolic phase profiles have demonstrated diffraction-limited focusing performance.[23] In addition, multiplexed metasurfaces operating across wavelength, polarization, and incidence angle enable multiple optical functions to be integrated on a single platform.[3,11,24–29]

Despite these advances, the large-scale practical deployment of metasurfaces remains limited by mechanical stability and environmental sensitivity. Metasurfaces typically rely on high-aspect-ratio nanostructures that are susceptible to damage during processing, cleaning, or maintenance. Nanostructures with a larger aspect ratio enable broader phase coverage and greater flexibility in optical modulation; however, this increased aspect ratio also leads to higher mechanical vulnerability. Holey metasurface designs have been proposed to improve mechanical robustness; however, they remain sensitive to external mechanical and environmental stresses, particularly during surface cleaning.[30]

Furthermore, conventional metasurfaces composed of nanopillar structures are directly exposed to air, which exhibit an optical response that is intrinsically sensitive to the refractive index of the surrounding medium. When the environmental medium changes, the effective refractive index of the meta-atoms shifts, inducing phase deviations from the designed optical phase profiles. This inherent environmental sensitivity restricts their practical operation to a single specific medium, complicating their application in integrated photonic systems, oil-immersed lenses,[31] and underwater lenses.[32]

Metasurfaces are regarded as reciprocal optical elements and are expected to exhibit symmetric bidirectional characteristics.[33] However, their typical configuration—an asymmetric stack consisting of air, nanostructures, and a substrate—introduces inherent asymmetry along the out-of-plane direction. This vertical asymmetry in both structure and

material composition leads to direction-dependent optical responses. Such effects become particularly significant in nonlinear or anisotropic systems,[34–36] where forward and backward incidences can induce distinct optical responses. Several recent studies have explored direction-dependent functionalities and incidence-direction multiplexing based on this asymmetry.[33,37] In contrast, enhancing the vertical symmetry of the structural design can improve the consistency of bidirectional optical responses, which is crucial for practical applications, such as imaging, optical communication, and integrated photonics.

To address these limitations, we report a robust CMOS-compatible embedded metasurface architecture realized by encapsulating high-index nanopillars within a conformal $\mathbf{SiO_2}$ matrix. An overview of the proposed concept is shown in **Figure 1.** This embedded design enhances structural robustness while preserving optical performance. Diffraction-limited focusing and high-resolution imaging are preserved, while optical throughput remains stable after mechanical cleaning. The near-symmetric embedding further enhances orientation-independent bidirectional imaging.

Although some materials have already been used as cladding layers in metasurface research, such as SU-8, SiN_x, and SiO_2, their role in improving structural durability under practical mechanical stresses has not been systematically quantified. For example, SiN_x has been used to reduce reflection and enhance broadband absorption,[38] SU-8 to reduce reflection,[39] and SiO_2 to protect optical transmission from environmental changes.[40] Here, we show that the embedded metasurface retains over 90% of its focusing efficiency after mechanical cleaning, whereas unprotected structures suffer efficiency losses of up to 88%. Although we demonstrate this approach using amorphous silicon (a-Si), the encapsulation strategy is applicable to other high-index materials such as TiO_2, GaN, diamond, and SiC.[41-43] These materials ($n > 2$) maintain full 2π phase control even when clad with SiO_2 ($n \approx 1.45$), and the small thermal expansion mismatch ($<5 \times 10^{-6}$/K) minimizes interfacial stress.

The subsequent sections detail the metasurface design methodology, and optical characterization. Comparative measurements highlight the improved durability and performance stability relative to pillar-based designs. Finally, orientation-independent behavior is validated through resolution tests and biological imaging experiments. These findings support the development of durable, alignment-tolerant metasurfaces suitable for integration into practical optical systems.

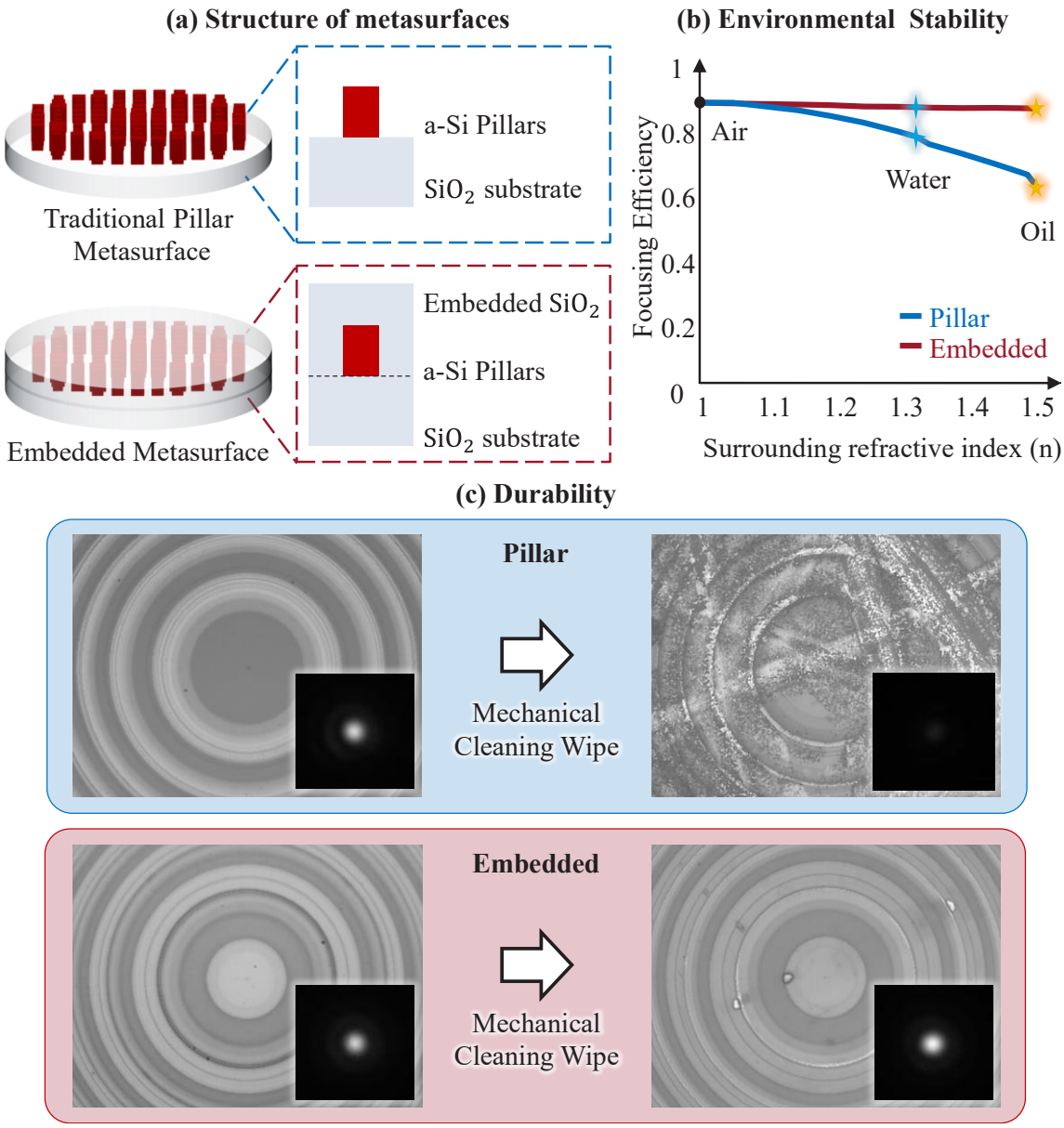

Figure 1. Design and environmental stability of embedded metasurfaces. (a) diagrams of a conventional pillar-based metasurface (top) and the embedded metasurface (bottom). (b) Simulated focusing efficiency of the two metasurfaces as a function of the surrounding refractive index (*n*), where the embedded metasurface maintains stable focusing efficiency. (c) Optical microscope images of the metasurfaces before and after mechanical cleaning, demonstrating structural durability of the embedded design.

2. Material Selection and Environmental Stability

Figure 1 (a) illustrates the structure of the proposed embedded metasurface architecture. The embedded metasurface consists of periodically arranged amorphous silicon pillars (a-Si) on a SiO_2 substrate, with a 2 μm-thick SiO_2 layer filling the gaps between the pillars and covering

the top surface to enhance device robustness. A-Si exhibits a high refractive index value and low loss in the near infrared spectrum.[41] SU-8 polymer has been utilized as a cladding material to enable double-sided metasurface structures.[39] However, its relatively high refractive index (1.6-1.7) limits the achievable 0–2π phase coverage for many high-index materials, such as Si_3N_4 and TiO_2. In contrast, SiO_2 offers a low refractive index (~1.45), ensuring sufficient index contrast for full 2π phase modulation while maintaining high transmission due to negligible optical absorption. In addition, the thermal expansion coefficient of SiO_2 is compatible with silicon-based fabrication processes, which minimizes intrinsic stress. The deposition of SiO_2 layers is fully CMOS-compatible, facilitating large-scale, low-cost, and highly stable component fabrication. Using SiO_2 as both the bottom substrate and the top encapsulation layer establishes a vertically symmetric dielectric environment. This symmetry is essential for achieving consistent optical transmission in both forward and backward directions and plays a key role in preserving bidirectional performance. The metasurface operates based on the propagation phase mechanism, in which the required phase delay is accumulated as light propagates through the nanopillars. Filling the gaps with SiO_2 does not affect the working mechanism, because the refractive index of the pillar material remains higher than that of SiO_2. In the conventional design, the gaps were filled with air (n = 1), whereas in the embedded design they are replaced by SiO_2. For a dielectric metasurface with thickness H and effective refractive index n_{eff}, the propagation phase is given by $\phi = \frac{2\pi}{\lambda} n_{eff} H$, where λ is the wavelength of the incident light. Based on this phase modulation model, the replacement of the surrounding medium primarily results in a change in the effective refractive index n_{eff}.

Full-lens finite-difference time-domain (FDTD) simulations were performed for both the embedded and conventional pillar-based designs to evaluate their optical performance under varying surrounding refractive indices. Both metasurfaces were designed with a diameter of 30 μm and a focal length of 60 μm, corresponding to a numerical aperture (NA) of 0.24, consistent with the fabricated devices. The meta-atom libraries used for two designs are detailed in Supporting Information S1. For the embedded configuration, the nanopillars were encapsulated within a 2 μm-thick SiO_2 cladding layer. Perfectly matched layers (PMLs) were applied in all directions. A linearly x-polarized plane wave at 808 nm was incident from the substrate side, and the electric-field distribution was recorded using frequency-domain field and power monitors placed in the xy-plane at z = 5 μm, with the same monitoring configuration applied in all simulations. Far-field projections along the propagation axis (z-

direction) were subsequently calculated, as shown in **Figure 2 (a)**. The surrounding refractive index varied from 1.0 (air) to 1.515 (oil) to represent typical operating environments.

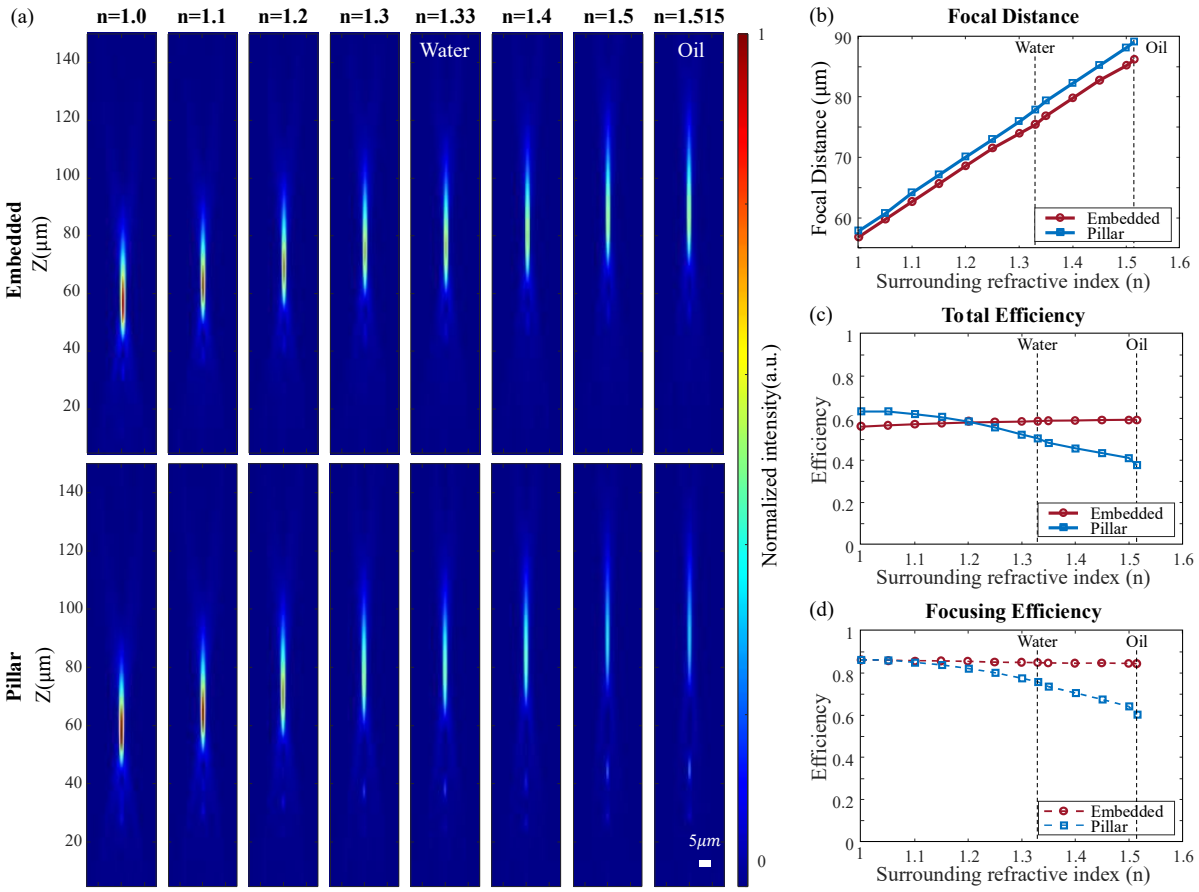

Figure 2. Optical performance of metasurfaces under varying surrounding refractive index. (a) Simulated electric-field intensity distributions for the embedded (top) and pillar-based (bottom) metasurfaces at different surrounding refractive indices (n = 1.0–1.515). (b) Focal distance as a function of the surrounding refractive index. (c) Total efficiency (solid lines) and (d) focusing efficiency (dashed lines) for the two metasurface designs under different surrounding refractive indices.

Both metasurfaces exhibit distinct focal spots over the entire range of surrounding refractive index. However, a significant degradation in the intensity of the focal point was observed with increasing refractive index, particularly for the pillar-based design. Although the designed focal length was fixed at 60 μm, both devices exhibited focal shifts as the environmental refractive index increased. This behavior arises from changes in the optical path length ($OPL = n \cdot s$) during propagation, where s is the path of geometrical length. Figure 2 (b) quantifies the focal shifts. The embedded metasurface shows a smaller shift and a more stable

focal shift, which is attributed to the effective isolation of the phase modulation elements by the SiO_2 encapsulation. In contrast, the pillar-based metasurface, with nanostructures directly exposed to the surrounding medium, exhibits larger deviations due to direct environmental modulation of the local effective refractive index and corresponding phase profile. The focusing and total efficiencies of both designs are presented in Figure 2 (c) and (d). The focusing efficiency (dashed lines) is defined as the ratio of the optical power within a circular aperture at the focal plane (diameter = 3 × FWHM of the focal spot) to total transmitted power. The total efficiency (solid lines) is defined as the ratio of the optical power within the same focal-plane aperture to the incident optical power. The embedded metasurface maintains high focusing efficiencies and total efficiencies across the full refractive-index range, whereas the focusing efficiency of the pillar-based design decreases from 86% to 60%. These results indicate that the embedded design preserves phase modulation capability and optical performance under realistic operational environments, including immersion in water or oil.

3. Optical Characterization and Mechanical Durability

To characterize the optical performance of the embedded metasurface, we measured the focusing process to quantify the focal length, depth of focus, and focal-spot size. The experimental setup consists of an 808 nm laser, adjustable mirrors, the metasurface, and a microscope system. In the microscope system, the light is collected by an objective lens and then passes through the tube lens to a camera. The horizontal microscope system was calibrated by using a USAF resolution target, resulting in an effective magnification of 43.3× with a 50× objective lens (NA = 0.45) and a tube lens (focal length = 200 mm).

In the characterization experiment, we first measured the optical performance of both the pillar-based metasurface (**Figure 3 (a)**) and the embedded metasurface (Figure 3 (c)), which were fabricated in the same run. To replicate practical conditions, a cleaning procedure was applied by gently wiping the metasurface surface with optical lens tissue. Following this, the optical performance of the metasurfaces was re-evaluated to enable a direct comparison before and after cleaning.

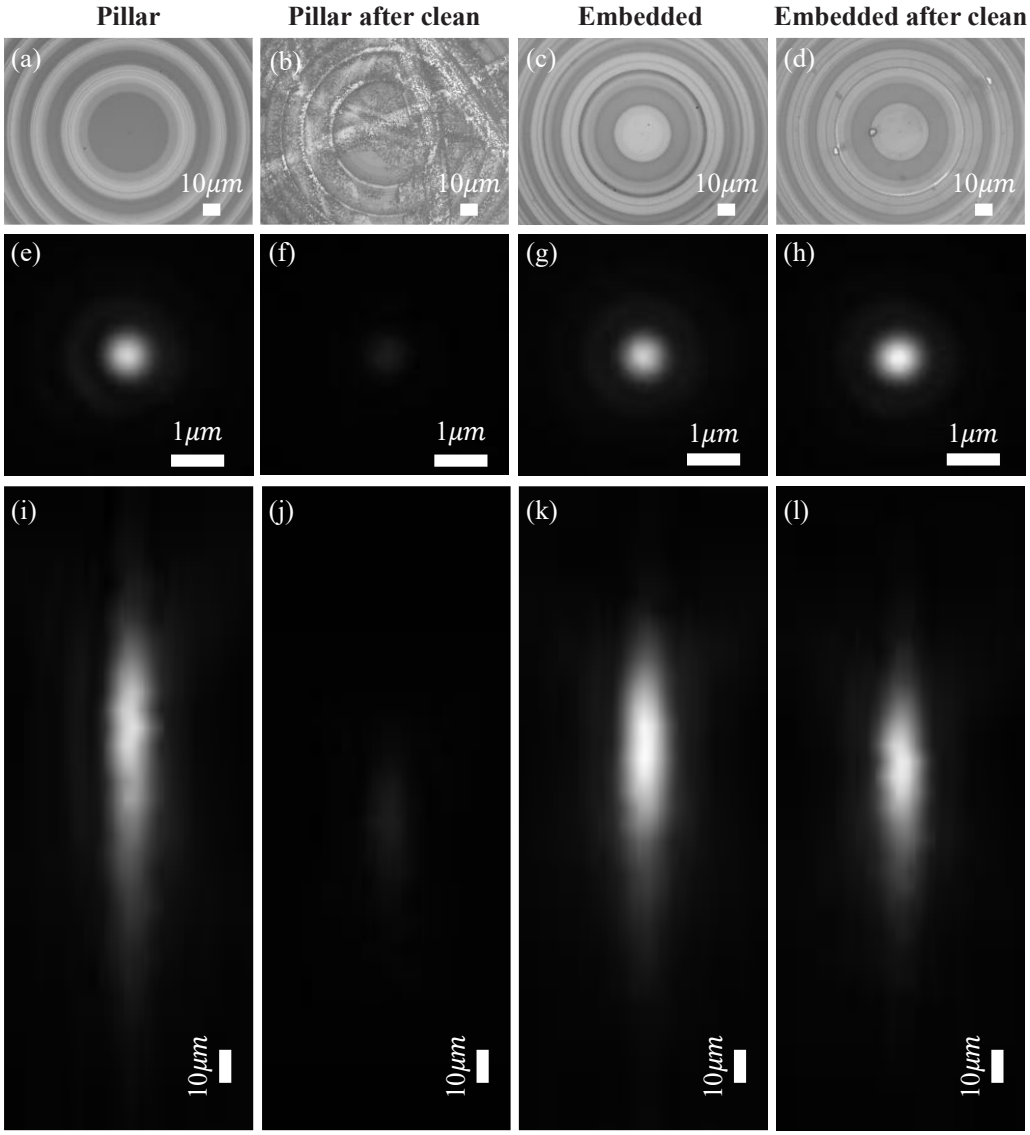

Figure 3. Optical characterization of pillar based metasurface and embedded metasurface. (a–d) Optical microscope images of the pillar-based (a,b) and embedded (c,d) metasurfaces before and after cleaning. (e–h) Focal spots in the xy-plane for the pillar-based (e,f) and embedded (g,h) metasurfaces before and after cleaning. (i–l) Focal spots in the xz-plane for the pillar-based (i,j) and embedded (k,l) metasurfaces before and after cleaning

The measured focal lengths were 1.181 mm (pillar-based) and 1.178 mm (embedded), both of which are close to the designed focal length of 1.2 mm, with relative errors of 1.58% and 1.83%, respectively (Figure 3 (e) and (g)). The full width at half maximum (FWHM) is 1.68 μm for both metasurfaces, which confirms that both designs achieve near-diffraction-limited focusing performance (1.68 μm). As shown in Figure 3 (i) and (k), the depth of focus is approximately 165 μm for both metasurfaces. These results indicate that the encapsulation process does not degrade optical performance.

Figure 3 (b) and (d) show optical microscope images of the metasurfaces after the cleaning procedure. Visible structural damage is observed in the pillar-based metasurface (Figure 3 (b)). The pillar-based metasurface exhibits severe surface scratches and partial loss or displacement of the patterns. In contrast, the embedded metasurface (Figure 3 (d)) maintains its structural integrity and exhibits no visible scratches.

To evaluate the impact of the cleaning process and structural damage on optical performance, we measured the focusing performance of the metasurfaces following the same procedure as before. The focal distance after cleaning was 1.179 mm for the pillar-based metasurface and 1.182 mm for the embedded metasurface, both of which remain consistent with their pre-cleaning values. This indicates that the previously observed difference in focal distances resulted from slight mechanical misalignment during the measurement. Similarly, the FWHM of the focal spots exhibits negligible changes compared to their pre-cleaning results. However, a critical disparity is observed in the optical throughput. To achieve comparable focal spot brightness, the embedded metasurface maintains high efficiency with an exposure time of 0.47 ms, while the pillar-based metasurface requires an exposure time of 4.11 ms under the same illumination conditions. Figure 3 (f) and (j) show the focal spots and depth-of-focus profiles along the z-direction, respectively, acquired at the same exposure time of 0.47 ms. The image of the pillar-based metasurface obtained with a 4.11 ms exposure time is provided in the Supporting Information Figure S5. Based on this exposure time ratio, the focus efficiency of the pillar-based design is reduced by approximately 88.6% compared to the embedded metasurface. The reduction indicates that mechanical damage degrades the optical performance of the pillar-based design. In contrast, the embedded metasurface preserves optical performance and mechanical robustness, demonstrating the effective protection provided by the SiO_2 layer.

4. Imaging Resolution and Biological Application

To evaluate the imaging capabilities and mechanical durability of the metasurfaces, we conducted comparative imaging experiments on both metasurfaces before and after the cleaning process. In these experiments, we performed resolution testing using a high-resolution USAF test target (TC-RT01, Edmund Optics) and conducted biological imaging of dragonfly wings to discuss the practical imaging performance across different applications. These comparative results provide insight into the mechanical durability and imaging reliability of the embedded design compared with the pillar-based metasurface. The experimental setup, designed for singlet metasurface imaging, is schematically shown in

Figure 4 (a) and (b). The object is illuminated by an incoherent 808 nm LED source through a condenser lens. The metasurface is used to form an image of the USAF resolution target located on one side of the structure onto the opposite side. The image is subsequently collected by the microscope system. Based on the actual dimension of the USAF resolution target image, the system magnification was calibrated to be 47×.

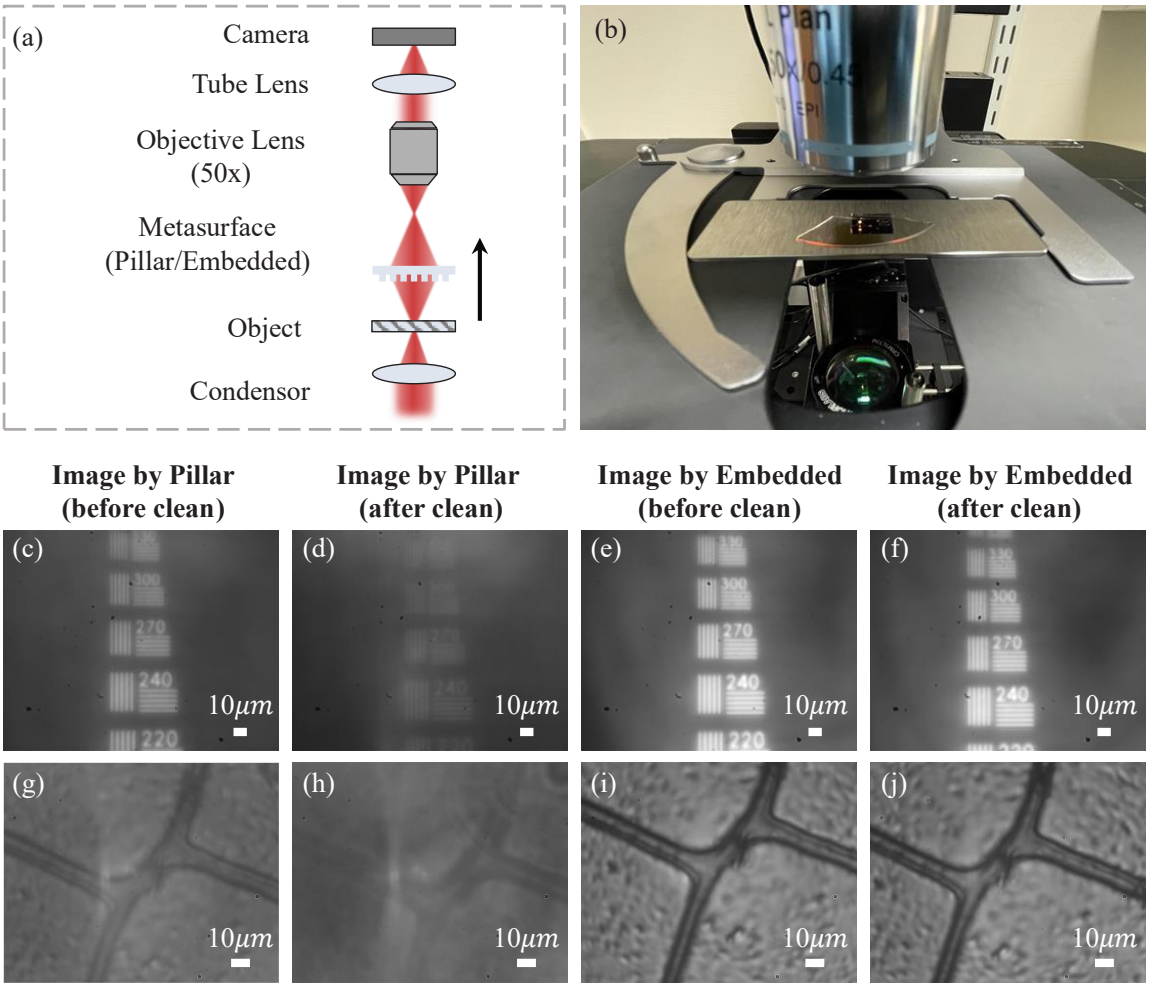

Figure 4. Imaging experiment with the pillar-based and embedded metasurface. (a) optical configuration of the imaging system. (b) imaging setup. (c)-(f) Imaging results of a USAF resolution target obtained using different metasurfaces: (c) pillar-based metasurface, (d) embedded metsurface, (e) pillar based metasurface after clean, and (f) embedded metasurface after clean. (g)-(j) Biological imaging results of dragonfly wings obtained using: (g) pillar based metasurface, (h) embedded metasurface, (i) pillar based metasurface after clean, and (j) embedded metasurface after clean, respectively.

We first quantified the spatial resolution limit using the USAF target. As shown in Figure 4 (c) and (e), prior to any mechanical cleaning, both the pillar-based and embedded

metasurfaces successfully resolve Group 330 (element frequency = 330 lp/mm). This corresponds to a resolvable line width of approximately 1.74 μm, which approaches the theoretical diffraction-limited resolution of 1.68 μm. Before cleaning, the embedded metasurface exhibits higher image quality than the pillar-based metasurface. Quantitative analysis using the Michelson contrast metric $C_{Michelson} = \frac{I_{max}-I_{min}}{I_{max}+I_{min}}$ demonstrates that the pillar-based metasurface achieves a contrast of 0.1 at the resolution limit (330 lp/mm), while the embedded metasurface reaches a contrast of 0.2. This enhancement suggests that the planarized surface effectively suppresses stray light scattering.

To assess mechanical durability, both metasurfaces were subjected to a cleaning protocol involving mechanical wiping with isopropyl alcohol (IPA) using optical lens tissue. Post-cleaning imaging was performed at the same location on the USAF target to ensure consistency. The results are shown in Figure 4 (d) and (f). Both devices exhibit a reduction in imaging quality after cleaning; however, the pillar-based metasurface exhibits a greater degree of degradation. In contrast, the embedded design displays only a slight change in performance, indicating improved resistance to mechanical damage. Quantitative analysis of Michelson contrast at Group 330 reveals a sharp decrease from 0.1 to 0.023 for the pillar-based metasurface, whereas the embedded design retains a much higher contrast of 0.17. This 77% reduction in contrast correlates with the structural damage and efficiency loss observed in Section 3. This result is consistent with the focal spot characterization results presented earlier, supporting the assessment of enhanced mechanical robustness in the embedded design.

In addition, biological imaging experiments with dragonfly wings demonstrate the practical imaging capabilities of both metasurface designs with the same singlet metasurface setup. As shown in Figure 4 (g)–(j), the imaging results of dragonfly wings are presented for the pillar-based metasurface, embedded metasurface, and their corresponding post-cleaning conditions. The embedded metasurface consistently resolves fine structural details with high fidelity throughout the test. In contrast, the pillar-based metasurface exhibits a noticeable reduction in image quality following the cleaning process, with blurring particularly at the edges of the sample. These results demonstrate that the embedded architecture ensures reliable, high-contrast imaging performance suitable for real applications.

5. Verification of Bidirectional Optical Symmetry

To investigate the bidirectional optical symmetry enabled by the symmetric dielectric environment, we conducted imaging experiments under two distinct configurations: wafer-up

(light incident from the substrate side) and wafer-down (light incident from the encapsulation side). **Figure 5(a) and (b)** show the optical setup, which is consistent with the singlet imaging system used previously. In both cases, the illumination source and the USAF resolution target are kept fixed. Additionally, the metasurface forms a projected image of the target on the opposite side, which is collected by the microscope system. The only difference between the two setups is the physical orientation of the metasurface relative to the object.

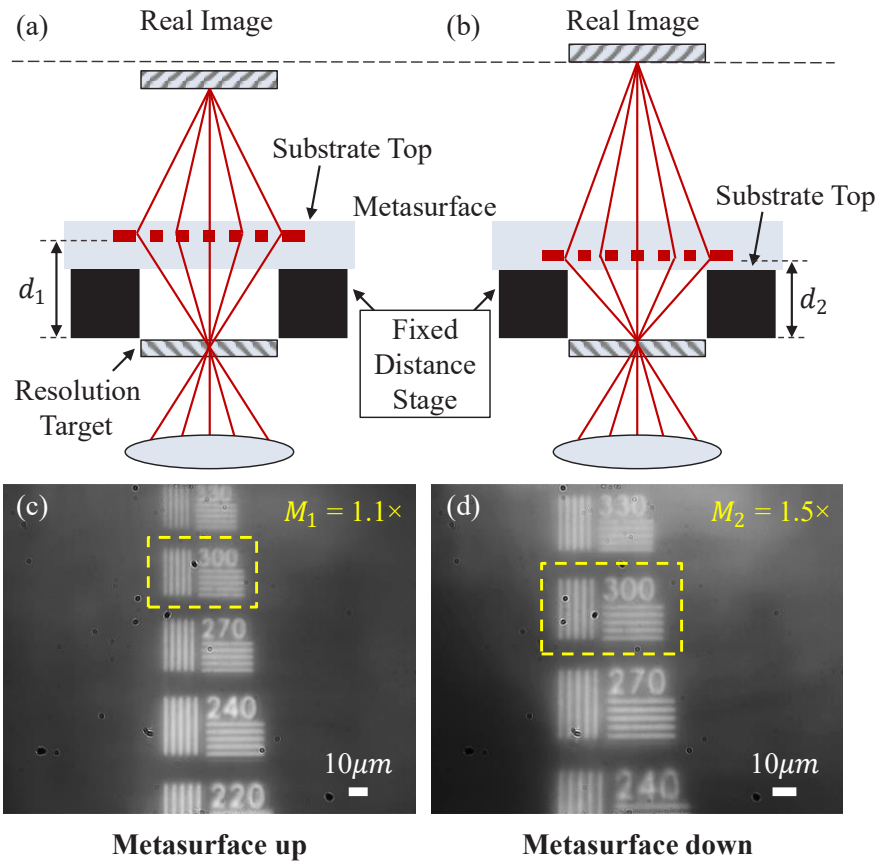

Figure 5. Bidirectional imaging experiment using wafer-down and wafer-up configurations. Schematic diagrams of the optical setups corresponding to the two configurations: (a) wafer-up setup, and (b) wafer-down setup. (c,d) Experimental imaging results of the same USAF resolution target obtained under the (c) wafer-up and (d) wafer-down setups, respectively.

Figures 5(c) and (d) show the imaging results of the same USAF target obtained under the wafer-up and wafer-down configurations, respectively. Both configurations produce images with comparable resolution and contrast, which confirms that the embedded metasurface exhibits orientation-independent optical behavior regardless of its orientation.

This orientation-independent behavior is a direct consequence of the SiO_2 encapsulation, which homogenizes the refractive index on both sides of the nanostructures and eliminates the interfacial phase discontinuities typically observed in air-clad designs.

A discrepancy in the field of view (FOV) and system magnification is observed between the two orientations, although similar line pairs are resolved. The wafer-up configuration exhibits a larger FOV and lower magnification than the wafer-down case. This variation is geometric and arises from differences in object distance caused by the thickness of the substrate. In the wafer-up configuration, the metasurface is farther from the sample, resulting in a longer object distance of approximately 1.5 mm (1.2 mm + 0.3 mm). In contrast, in the wafer-down configuration, the metasurface is placed much closer to the sample, with an object distance of approximately 1.2mm (1.2 mm + 0.000155 mm). The shorter object distance in the wafer-down configuration leads to a higher magnification and correspondingly smaller field of view. Based on the thin-lens equation, the corresponding image distances are calculated to be 2.51 mm and 2.999 mm for the wafer-up and wafer-down configurations, respectively. These result in theoretical single-lens magnifications of 1.1× and 1.5×. This yields a theoretical magnification ratio of 1.36. Experimentally, a magnification ratio of 1.29 is observed, corresponding to a relative error of ~5%, which is within experimental uncertainty. These quantitative results confirm that the observed scaling difference is fully explained by the geometric variation in object distance, rather than a change in the intrinsic optical response of the metasurface. Consequently, the embedded metasurface demonstrates robust, orientation-independent functionality, making it highly suitable for integration into bidirectional optical systems.

6. Conclusion

In conclusion, a mechanically robust embedded metasurface architecture has been demonstrated that effectively overcomes the intrinsic fragility and environmental sensitivity of traditional pillar-based designs. Numerical simulations confirm stable focusing efficiency across a broad refractive index range (n = 1.0-1.515), indicating compatibility with diverse immersion media including water and oil. By encapsulating high-index nanostructures within a conformal SiO_2 cladding, the embedded configuration preserves diffraction-limited focusing and imaging performance while exhibiting improved mechanical durability. Crucially, experimental validation reveals that the embedded metasurface retains more than 90% of its optical efficiency following standard mechanical cleaning, in contrast to the efficiency reduction of approximately 88% observed in unprotected designs. In addition, the symmetric

dielectric environment eliminates structural asymmetry and enables orientation-independent bidirectional imaging capabilities. This facilitates bidirectional imaging performance without the need for orientation-dependent alignment and simplifies system integration. The embedded metasurface offers the potential for practical implementation of robust metasurfaces in future large-scale applications. Future work may explore the extension of this embedding approach to dynamic or multifunctional metasurfaces, advancing toward deployable, multifunctional flat optical systems.

Acknowledgements

This work was supported by the UK's Engineering and Physical Sciences Research Council (project number EP/V000624/1, EP/X041166/1, and UKRI257).

References

1. Arbabi, Amir, Ehsan Arbabi, Seyedeh Mahsa Kamali, Yu Horie, Seunghoon Han, and Andrei Faraon. 2016. 'Miniature Optical Planar Camera Based on a Wide-Angle Metasurface Doublet Corrected for Monochromatic Aberrations'. *Nature Communications* 7 (1): 13682. https://doi.org/10.1038/ncomms13682.
2. Arbabi, Amir, Yu Horie, Mahmood Bagheri, and Andrei Faraon. 2015. 'Dielectric Metasurfaces for Complete Control of Phase and Polarization with Subwavelength Spatial Resolution and High Transmission'. *Nature Nanotechnology* 10 (11): 937–43. https://doi.org/10.1038/nnano.2015.186.
3. Avayu, Ori, Euclides Almeida, Yehiam Prior, and Tal Ellenbogen. 2017. 'Composite Functional Metasurfaces for Multispectral Achromatic Optics'. *Nature Communications* 8 (1): 14992. https://doi.org/10.1038/ncomms14992.
4. Balthasar Mueller, J. P., Noah A. Rubin, Robert C. Devlin, Benedikt Groever, and Federico Capasso. 2017. 'Metasurface Polarization Optics: Independent Phase Control of Arbitrary Orthogonal States of Polarization'. *Physical Review Letters* 118 (11): 113901. https://doi.org/10.1103/PhysRevLett.118.113901.
5. Bao, Yanjun, Ying Yu, Haofei Xu, et al. 2018. 'Coherent Pixel Design of Metasurfaces for Multidimensional Optical Control of Multiple Printing-Image Switching and Encoding'. *Advanced Functional Materials* 28 (51): 1805306. https://doi.org/10.1002/adfm.201805306.

6. Basilio-Ortiz, J Carlos, and Ivan Moreno. n.d. *Unveiling Invariant Optical Properties of Dielectric Meta-Atoms*.
7. Chen, Boqu, Xiaoyu Sun, Xiaoxuan Li, et al. 2025. '4H-SiC Metalens: Mitigating Thermal Drift Effect in High-Power Laser Irradiation'. *Advanced Materials* 37 (3): 2412414. https://doi.org/10.1002/adma.202412414.
8. Chen, Ke, Guowen Ding, Guangwei Hu, et al. 2020. 'Directional Janus Metasurface'. *Advanced Materials* 32 (2): 1906352. https://doi.org/10.1002/adma.201906352.
9. Chen, Ke, and Yijun Feng. 2022. 'A Review of Recent Progress on Directional Metasurfaces: Concept, Design, and Application'. *Journal of Physics D: Applied Physics* 55 (38): 383001. https://doi.org/10.1088/1361-6463/ac7e04.
10. Chen, Xianzhong, Yan Zhang, Lingling Huang, and Shuang Zhang. 2014. 'Ultrathin Metasurface Laser Beam Shaper'. *Advanced Optical Materials* 2 (10): 978–82. https://doi.org/10.1002/adom.201400186.
11. Fan, Qingbin, Daopeng Wang, Pengcheng Huo, Zijie Zhang, Yuzhang Liang, and Ting Xu. 2017. 'Autofocusing Airy Beams Generated by All-Dielectric Metasurface for Visible Light'. *Optics Express* 25 (8): 9285–94. https://doi.org/10.1364/OE.25.009285.
12. Faraji-Dana, MohammadSadegh, Ehsan Arbabi, Amir Arbabi, Seyedeh Mahsa Kamali, Hyounghan Kwon, and Andrei Faraon. 2018. 'Compact Folded Metasurface Spectrometer'. *Nature Communications* 9 (1): 4196. https://doi.org/10.1038/s41467-018-06495-5.
13. Geromel, René, Christian Weinberger, Katja Brormann, Michael Tiemann, and Thomas Zentgraf. 2022. 'Porous SiO_2 Coated Dielectric Metasurface with Consistent Performance Independent of Environmental Conditions'. *Optical Materials Express* 12 (1): 13–21. https://doi.org/10.1364/OME.444264.
14. Hsu, Wei-Lun, Yen-Chun Chen, Shang Ping Yeh, Qiu-Chun Zeng, Yao-Wei Huang, and Chih-Ming Wang. 2022. 'Review of Metasurfaces and Metadevices: Advantages of Different Materials and Fabrications'. *Nanomaterials* 12 (12): 12. https://doi.org/10.3390/nano12121973.
15. Huang, Yao-Wei, Wei Ting Chen, Wei-Yi Tsai, et al. 2015. 'Aluminum Plasmonic Multicolor Meta-Hologram'. *Nano Letters* 15 (5): 3122–27. https://doi.org/10.1021/acs.nanolett.5b00184.
16. Jang, Mooseok, Yu Horie, Atsushi Shibukawa, et al. 2018. 'Wavefront Shaping with Disorder-Engineered Metasurfaces'. *Nature Photonics* 12 (2): 84–90. https://doi.org/10.1038/s41566-017-0078-z.

17. Kamali, Seyedeh Mahsa, Ehsan Arbabi, Amir Arbabi, Yu Horie, MohammadSadegh Faraji-Dana, and Andrei Faraon. 2017. ‘Angle-Multiplexed Metasurfaces: Encoding Independent Wavefronts in a Single Metasurface under Different Illumination Angles’. *Physical Review X* 7 (4): 041056. https://doi.org/10.1103/PhysRevX.7.041056.
18. Khorasaninejad, M., W. T. Chen, J. Oh, and F. Capasso. 2016. ‘Super-Dispersive Off-Axis Meta-Lenses for Compact High Resolution Spectroscopy’. *Nano Letters* 16 (6): 3732–37. https://doi.org/10.1021/acs.nanolett.6b01097.
19. Khorasaninejad, Mohammadreza, Wei Ting Chen, Robert C. Devlin, Jaewon Oh, Alexander Y. Zhu, and Federico Capasso. 2016. ‘Metalenses at Visible Wavelengths: Diffraction-Limited Focusing and Subwavelength Resolution Imaging’. *Science* 352 (6290): 1190–94. https://doi.org/10.1126/science.aaf6644.
20. Khorasaninejad, Mohammadreza, and Kenneth B. Crozier. 2014. ‘Silicon Nanofin Grating as a Miniature Chirality-Distinguishing Beam-Splitter’. *Nature Communications* 5 (1): 5386. https://doi.org/10.1038/ncomms6386.
21. Lawrence, Mark, David R. III Barton, and Jennifer A. Dionne. 2018. ‘Nonreciprocal Flat Optics with Silicon Metasurfaces’. *Nano Letters* 18 (2): 1104–9. https://doi.org/10.1021/acs.nanolett.7b04646.
22. Lim, Soon Wei Daniel, Maryna L. Meretska, and Federico Capasso. 2021. ‘A High Aspect Ratio Inverse-Designed Holey Metalens’. *Nano Letters* 21 (20): 8642–49. https://doi.org/10.1021/acs.nanolett.1c02612.
23. Liu, Xiaoyuan, Mu Ku Chen, Cheng Hung Chu, et al. 2023. ‘Underwater Binocular Meta-Lens’. *ACS Photonics* 10 (7): 2382–89. https://doi.org/10.1021/acsphotonics.2c01667.
24. Luo, Jun, Zuojun Zhang, Maowen Song, Anguo He, and Honglin Yu. 2017. ‘Simultaneous Generation and Focus of Radially Polarized Light with Metal-Dielectric Grating Metasurface’. *Optics Communications* 382 (January): 421–27. https://doi.org/10.1016/j.optcom.2016.07.015.
25. Minovich, Alexander E., Andrey E. Miroshnichenko, Anton Y. Bykov, Tatiana V. Murzina, Dragomir N. Neshev, and Yuri S. Kivshar. 2015. ‘Functional and Nonlinear Optical Metasurfaces’. *Laser & Photonics Reviews* 9 (2): 195–213. https://doi.org/10.1002/lpor.201400402.
26. Ni, Xingjie, Alexander V. Kildishev, and Vladimir M. Shalaev. 2013. ‘Metasurface Holograms for Visible Light’. *Nature Communications* 4 (1): 2807. https://doi.org/10.1038/ncomms3807.

27. Tittl, Andreas, Aleksandrs Leitis, Mingkai Liu, et al. 2018. ‘Imaging-Based Molecular Barcoding with Pixelated Dielectric Metasurfaces’. *Science* 360 (6393): 1105–9. https://doi.org/10.1126/science.aas9768.
28. Tripathi, Aditya, Chibuzor Fabian Ugwu, Viktar S. Asadchy, et al. 2024. ‘Nanoscale Optical Nonreciprocity with Nonlinear Metasurfaces’. *Nature Communications* 15 (1): 5077. https://doi.org/10.1038/s41467-024-49436-1.
29. Veksler, Dekel, Elhanan Maguid, Nir Shitrit, Dror Ozeri, Vladimir Kleiner, and Erez Hasman. 2015. ‘Multiple Wavefront Shaping by Metasurface Based on Mixed Random Antenna Groups’. *ACS Photonics* 2 (5): 661–67. https://doi.org/10.1021/acsphotonics.5b00113.
30. Wang, Bo, Fengliang Dong, Qi-Tong Li, et al. 2016. ‘Visible-Frequency Dielectric Metasurfaces for Multiwavelength Achromatic and Highly Dispersive Holograms’. *Nano Letters* 16 (8): 5235–40. https://doi.org/10.1021/acs.nanolett.6b02326.
31. Wang, Qiu, Xueqian Zhang, Yuehong Xu, et al. 2016. ‘Broadband Metasurface Holograms: Toward Complete Phase and Amplitude Engineering’. *Scientific Reports* 6 (1): 32867. https://doi.org/10.1038/srep32867.
32. Wang, Shuming, Pin Chieh Wu, Vin-Cent Su, et al. 2017. ‘Broadband Achromatic Optical Metasurface Devices’. *Nature Communications* 8 (1): 187. https://doi.org/10.1038/s41467-017-00166-7.
33. Wang, Shuming, Pin Chieh Wu, Vin-Cent Su, et al. 2018. ‘A Broadband Achromatic Metalens in the Visible’. *Nature Nanotechnology* 13 (3): 3. https://doi.org/10.1038/s41565-017-0052-4.
34. Wu, Shangliang, Yan Ye, Zhouying Jiang, Tianchi Yang, and Linsen Chen. 2019. ‘Large-Area, Ultrathin Metasurface Exhibiting Strong Unpolarized Ultrabroadband Absorption’. *Advanced Optical Materials* 7 (24): 1901162. https://doi.org/10.1002/adom.201901162.
35. Xiong, Bo, Yihao Xu, Jianan Wang, et al. 2021. ‘Realizing Colorful Holographic Mimicry by Metasurfaces’. *Advanced Materials* 33 (21): 2005864. https://doi.org/10.1002/adma.202005864.
36. Yang, Xun, Bo Wu, Pei-Pei Chen, et al. 2024. ‘Diamond Based Optical Metasurfaces for Broadband Wavefront Shaping in Harsh Environment’. *Laser & Photonics Reviews* 18 (9): 2400007. https://doi.org/10.1002/lpor.202400007.
37. Yu, Nanfang, and Federico Capasso. 2014. ‘Flat Optics with Designer Metasurfaces’. *Nature Materials* 13 (2): 139–50. https://doi.org/10.1038/nmat3839.

38. Yu, Nanfang, Patrice Genevet, Mikhail A. Kats, et al. 2011. ‘Light Propagation with Phase Discontinuities: Generalized Laws of Reflection and Refraction’. *Science* 334 (6054): 333–37. https://doi.org/10.1126/science.1210713.
39. Zhang, Lei, Shengtao Mei, Kun Huang, and Cheng-Wei Qiu. 2016. ‘Advances in Full Control of Electromagnetic Waves with Metasurfaces’. *Advanced Optical Materials* 4 (6): 818–33. https://doi.org/10.1002/adom.201500690.
40. Zhao, Zeyu, Mingbo Pu, Hui Gao, et al. 2015. ‘Multispectral Optical Metasurfaces Enabled by Achromatic Phase Transition’. *Scientific Reports* 5 (1): 15781. https://doi.org/10.1038/srep15781.
41. Zharov, Alexander, Vanessa Fierro, and Alain Celzard. 2023. ‘Non-Reciprocal Electromagnetic Metasurface Based on the Nonlinearity of a Liquid Metamaterial’. *Optics Letters* 48 (19): 5033–36. https://doi.org/10.1364/OL.500952.
42. Zhou, Yi, Rui Chen, and Yungui Ma. 2018. ‘Characteristic Analysis of Compact Spectrometer Based on Off-Axis Meta-Lens’. *Applied Sciences* 8 (3): 3. https://doi.org/10.3390/app8030321.
43. Zhu, Jia-Cheng, Jian-Kang Zhou, and Wei-Min Shen. 2019. ‘Polarisation-Independent Diffraction Grating Based on Dielectric Metasurface’. *Electronics Letters* 55 (13): 756–59. https://doi.org/10.1049/el.2019.1203.

Supporting Information

Supporting Information is available from the Wiley Online Library or from the author.